



Mo-doped BiVO₄ nanotextured pillars as efficient photoanodes for solar water splitting



Min-Woo Kim^{a,1}, Karam Kim^{a,1}, Tae Yoon Ohm^a, Bhavana Joshi^a, Edmund Samuel^a, Mark T. Swihart^b, Hyun Yoon^c, Hyunwoong Park^d, Sam S. Yoon^{a,*}

^a School of Mechanical Engineering, Korea University, Seoul, 136-713, Republic of Korea

^b Department of Chemical & Biological Engineering, University at Buffalo, The State University of New York, Buffalo, NY, 14260-4200, USA

^c KIER-UNIST Advanced Center for Energy, Korea Institute of Energy Research (KIER), 50, UNIST-gil, Ulsan, 44919, Republic of Korea

^d School of Energy Engineering, Kyungpook National University, Daegu, 41566, Republic of Korea

ARTICLE INFO

Article history:

Received 24 March 2017

Received in revised form

21 July 2017

Accepted 25 July 2017

Available online 29 July 2017

Keywords:

Bismuth vanadate

Nanotextured-pillar

Photoanode

Water splitting

Photocurrent density

ABSTRACT

We present electrospray-deposited nanotextured Mo-doped BiVO₄ pillars with improved photoelectrochemical water splitting performance. The three-dimensional nanotextured Mo-BiVO₄ pillars exhibit large interstitial spaces, which result in a high photocurrent. The doping of Mo at the optimal concentration (0.15%) results in a two-fold increase in the photocurrent density (PCD) (1.78 mA·cm⁻² at 1.2 V versus Ag/AgCl) over that of pristine BiVO₄. We attribute this increase in the PCD to increases in recombination time and in donor (electron) concentration owing to the doping with hexavalent Mo, as confirmed by Bode phase and Mott-Schottky analyses, respectively.

© 2017 Elsevier B.V. All rights reserved.

1. Introduction

The depletion of fossil fuel reserves and the concomitant increase in environmental pollution have galvanized efforts to develop environmentally friendly energy sources. One of the primary challenges in this regard is the conversion of solar energy into electricity or stored chemical energy [1,2]. Photocatalytic semiconductor materials absorb sunlight and can convert solar energy into chemical energy by splitting water into hydrogen and oxygen using photogenerated charge carriers [3–5].

Semiconductor metal oxides that exhibit an appropriate band gap energy are required for generating electron-hole pairs for photocatalysis [1,2,6,7]. Among the various semiconductor metal oxides being explored as photoanode materials for this purpose, n-type oxides show particular promise as materials suitable for oxygen evolution while p-type oxides are ideal for the hydrogen evolution component of water splitting. Bismuth vanadate (BiVO₄), which is an n-type material that can be used as a photoanode, is

chemically stable and shows high absorbance at visible light wavelengths, with a band gap of 2.4–2.6 eV. BiVO₄ has three crystalline phases. It can adopt tetragonal scheelite, monoclinic scheelite, and tetragonal zircon structures. The three-dimensional structure of BiVO₄ is formed by the coordination of an O atom with two Bi centers, with one V atom in the center holding them together. In the monoclinic scheelite structure, the local environments of the V and Bi ions are significantly distorted as compared to the tetragonal structure [8]. This distortion improves light absorption and electron-hole separation in monoclinic scheelite-like BiVO₄ [9].

Even though monoclinic scheelite-like BiVO₄ has a low band gap energy and shows a conduction band edge at 0 V (versus natural hydrogen electrode) at pH 0 [10], the water splitting activity of BiVO₄ is smaller than expected based upon its theoretical photocurrent density of 6.5 mA·cm⁻² [11]. This limited photoelectrochemical (PEC) performance of BiVO₄ is due to charge recombination that is promoted by its relatively low electron mobility and small hole diffusion length [12].

Various approaches have been reported for overcoming the above-mentioned challenges of charge recombination and increasing the lifetime of charge carriers, such as the formation of a

* Corresponding author.

E-mail address: skyoons@korea.ac.kr (S.S. Yoon).

¹ These authors have contributed equally.

heterostructure [13–15] or nanostructures [16,17] and doping [18–20]. Of these, doping is a particularly well-suited method. It is a straightforward process in which a small amount of an impurity is added to an intrinsic semiconductor to tune its properties, especially its optical and electronic properties [7,21]. Metal doping can enhance the photocatalytic performance of BiVO_4 and limit electron/hole recombination by increasing carrier concentration and mobility [22–24]. Dopants such as Na, Eu, Dy, Mo, Pd, and Si have been reported to enhance electron mobility as well as the PEC performance by increasing the electron density [19,25]. The doping of Mo in BiVO_4 occurs by substitution of V atoms with Mo, resulting in enhanced charge separation. Further, it has been reported that the amount of O_2 evolved during the solar oxidation of water using an electrospun Mo-doped BiVO_4 photoanode is greater than that produced using pristine BiVO_4 photoanode [24,26].

Some of the methods reported for doping Mo in BiVO_4 include spin coating [27], doctor blade coating [28], drop coating [19], and reactive sputtering [29]. However, there are no reports on the doping of Mo into BiVO_4 by electrostatic spray deposition (ESD), which is a nonvacuum, room-temperature deposition technique. In ESD, doping and band gap engineering can be realized by varying the composition of the solution that is electrospayed and the conditions for the post-deposition annealing process. ESD uses static electricity to transform a fluid into a spray of fine droplets, which is projected onto the target substrate. Because of the nano-scale dimensions of the droplets, nanostructured films that exhibit excellent adhesion and uniformity can be obtained [30].

In this work, we report the tailoring of the electron concentration of n-type Mo-doped BiVO_4 by ESD. Porous Mo-doped BiVO_4 films consisting of nanotextured pillars with large interstitial spaces are formed using the ESD process. Using various characterization techniques, we confirm the doping of Mo in BiVO_4 as well as its effect on the PEC performance. The results suggest that the observed improvement in the PEC performance is attributable to increases in the electron mobility and donor concentration.

2. Materials and methods

2.1. Fabrication of Mo-doped BiVO_4 films

The precursor solution for the Mo-doped BiVO_4 films was prepared by mixing 1.08 g of bismuth (III) nitrate pentahydrate ($\text{BiN}_3\text{O}_9 \cdot 5\text{H}_2\text{O}$, $\geq 98\%$, Sigma-Aldrich) and 0.78 g of vanadium (III) acetylacetonate ($\text{V}(\text{C}_5\text{H}_7\text{O}_2)_3$, Sigma-Aldrich) with acetic acid (CH_3COOH , 99.7%, 10 ml, Samchun Chemicals) at room temperature of 25 °C. Specific amounts of molybdenum(VI) oxide (MoO_3 , 99.5%, Sigma-Aldrich) were added to this BiVO_4 precursor solution, which was then stirred for 30 min. Mo was doped using concentrations corresponding to Mo/ BiVO_4 mole ratios of 0, 0.05, 0.1, 0.15, and 0.2%; the corresponding films are labeled as Mo-0, Mo-1, Mo-2, Mo-3, and Mo-4, respectively.

The Mo- BiVO_4 precursor solution was deposited on an indium tin oxide (ITO) glass substrate by electrostatic spraying for 60 min at a flow rate of 80 $\mu\text{l}/\text{h}$. A high voltage (10.5 kV) was applied to the nozzle, to ensure a stable Taylor cone. Fig. 1a shows a schematic of the ESD apparatus used. A cross-sectional scanning electron microscopy (SEM) image of an as-deposited BiVO_4 is shown in Fig. 1b, confirming that the film consists of nanotextured pillars.

2.2. Characterization of fabricated Mo-doped BiVO_4 films

An X-ray diffraction (XRD) system (D/max-2500, Rigaku, Japan) with a $\text{Cu-K}\alpha$ radiation source was used for analyzing the crystal structures of the Mo- BiVO_4 films; the scans were performed for 2θ values of 20–65°. X-ray photoelectron spectroscopy (XPS, Theta

Probe Base System, Thermo Fisher Scientific Co.) was used to determine the chemical compositions of the films. The morphologies of the Mo- BiVO_4 films were determined using a high-resolution SEM (HR-SEM) system (XL30 SFEG, Phillips Co., Holland) at 15 kV. The Raman scattering spectra of the Mo- BiVO_4 films were measured with a Raman spectrometer (LabRam ARAMIS IR2, Horiba Jobin Yvon) with a 532 nm laser source. The absorbance of the films was determined using an ultraviolet (UV)–visible spectrometer (Optizen POP Mecasys Co. Ltd, Korea).

2.3. Photoelectrochemical measurements

The PEC performances of the Mo- BiVO_4 films was determined through measurement of PCD during water splitting. The Mo- BiVO_4 film being tested was used as the working electrode, while an Ag/AgCl electrode was employed as the reference electrode and a piece of platinum wire as the counter electrode. The PEC measurements were performed in 0.5 M Na_2SO_4 as the electrolyte. A Xe arc lamp (Newport, Oriol Instruments, USA) equipped with an AM 1.5 filter was used to simulate sunlight. The PCD was measured using a potentiostat (VersaSTAT-3, Princeton Applied Research, USA) for applied voltages of –0.4 to 1.2 V (versus Ag/AgCl); the scan rate during the measurements was 10 mV/s. Electrochemical impedance spectroscopy (EIS) measurements were performed using the potentiostat mentioned above with the same electrode configuration. A small sinusoidal perturbation (amplitude of 10 mV) was added to the applied potential [31] within the frequency range of 100 kHz to 100 mHz under dark and illuminated conditions. The measurements were performed under dark conditions to obtain the Mott-Schottky plots.

3. Results and discussion

3.1. Film characterization

The cross-sectional morphologies of the different Mo-doped BiVO_4 films were examined by SEM, as shown in Fig. 2. In all the cases, the height of the pillars formed after deposition for 60 min was approximately 9 μm . As reported previously [23,32], the porous nature of these nanopillars increases the surface area of the films, making it greater than that of similar planar films. Further, it was observed that the nanopillars comprising the BiVO_4 films were unperturbed by doping with Mo. Finally, these images show that the pillars stand together and are plump in appearance, consisting of large numbers of nanosized BiVO_4 or Mo- BiVO_4 particles. The enhanced surface area should increase the number of reaction sites and reduce the transport distance for photogenerated electrons and holes to reach a reaction site, ultimately leading to the availability of a greater number of electrons and holes for reaction.

Fig. 3 shows a comparison of the XRD patterns of the Mo-doped BiVO_4 films deposited on ITO substrates using precursor solutions of various concentrations. In the case of the Mo-0 film (pure BiVO_4), BiVO_4 -related diffraction peaks are observed at 2θ values of 28.9, 30.8, 34.6, 35.3, 39.9, 42.6, 45.4, 47.2, 47.6, 50.5, 53.4, 56.5, 58.5, and 59.7°; these correspond to the (121), (040), (200), (020), (211), (051), $-(231)$, (240), (042), (202), (161), (251), (321), and (123) planes, respectively. The diffraction peaks confirmed that BiVO_4 exhibited the monoclinic scheelite-like structure (JCPDS No. 14-0688) [23,33,34]. ITO exhibits peaks at diffraction angles (2θ of 30.8, 35.3, 50.5, and 59.7°), similar to some of the BiVO_4 peaks; thus, the ITO-related peaks could not be distinguished easily. When Mo was doped in BiVO_4 , no secondary peaks or peaks related to MoO_3 were observed, confirming that all of the Mo had dissolved in the BiVO_4 . Further, the similarity in the XRD patterns of the pristine and Mo- BiVO_4 films confirmed that the monoclinic structure was

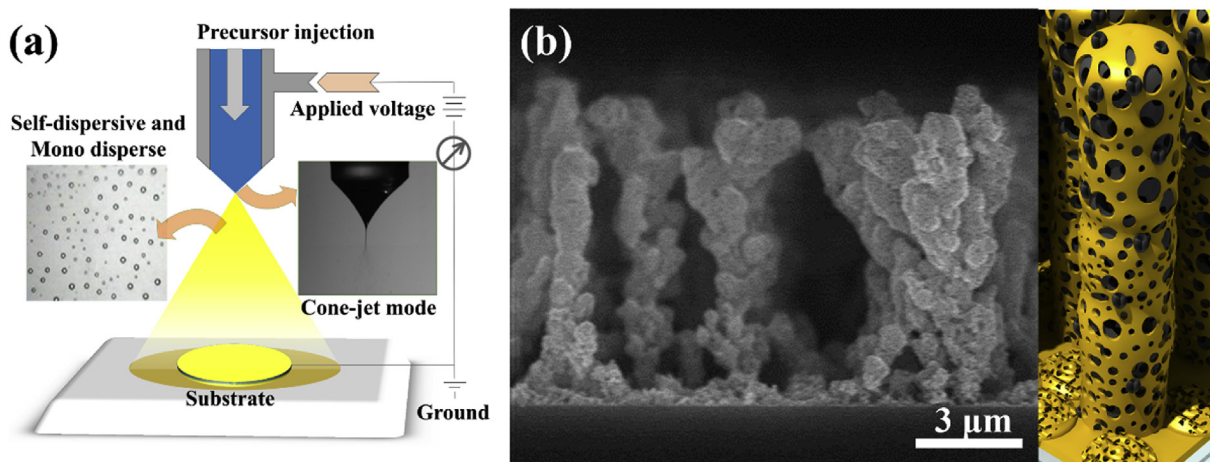


Fig. 1. (a) Schematic of electrostatic spray deposition and (b) nanotextured pillars of as-deposited Mo-BiVO₄ film.

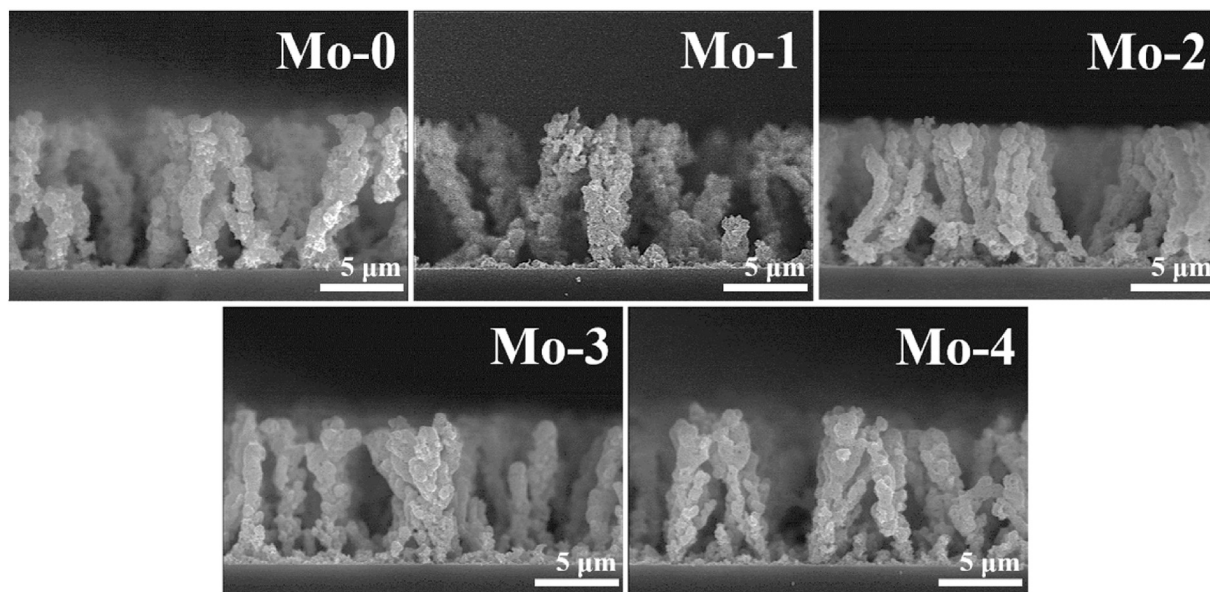


Fig. 2. Cross-sectional SEM images of Mo-doped BiVO₄ films with different Mo concentrations.

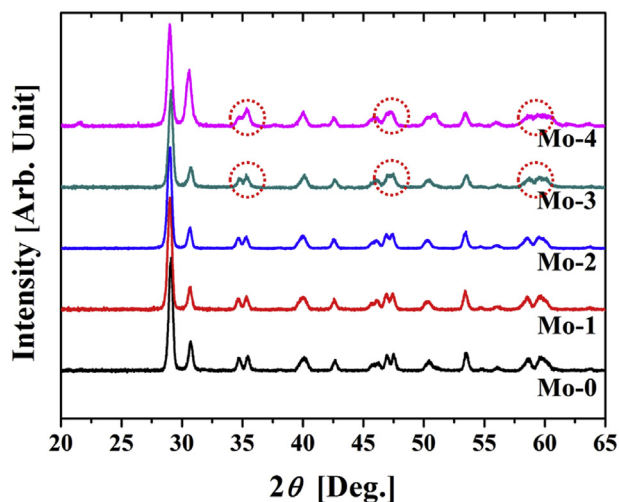


Fig. 3. XRD patterns of different Mo-doped BiVO₄ films.

maintained after the Mo doping. However, it appeared that the peaks at 34.6/35.3, 47.2/47.6, and 58.5/59.7° had merged in the case of the Mo-3 and Mo-4 films because the doping of Mo in large amounts led to the deformation of the scheelite-like structure. Further, the characteristic peak of BiVO₄ at 28.9° was shifted to a slightly higher diffraction angle. The shift was attributed to compressive strain induced by the incorporation of Mo⁺⁶ ions, which have a radius 0.055 nm, in place of smaller V⁺⁵ ions (radius of 0.05 nm). This observation is similar to that reported in previous studies [19,20,35].

Fig. 4a shows the Raman spectra of the Mo-0 and Mo-3 films. Raman bands can be observed at ~205, 330, 366, 715, and 818 cm⁻¹ for both films, corresponding to typical vibrations of monoclinic BiVO₄ [36,37]. The band at 205 cm⁻¹ can be assigned to the external modes (translation/rotation) of BiVO₄. Further, the peaks at approximately 330 and 366 cm⁻¹, are attributable to the asymmetric ($\delta_{as}(\text{VO}_4^{3-})$) and symmetric ($\delta_s(\text{VO}_4^{3-})$) deformation modes of VO₄³⁻, respectively. The dominant Raman band at 818 cm⁻¹ is related to the stretching mode of the V–O bond. However, the peak related to the V–O stretching mode is shifted to a lower

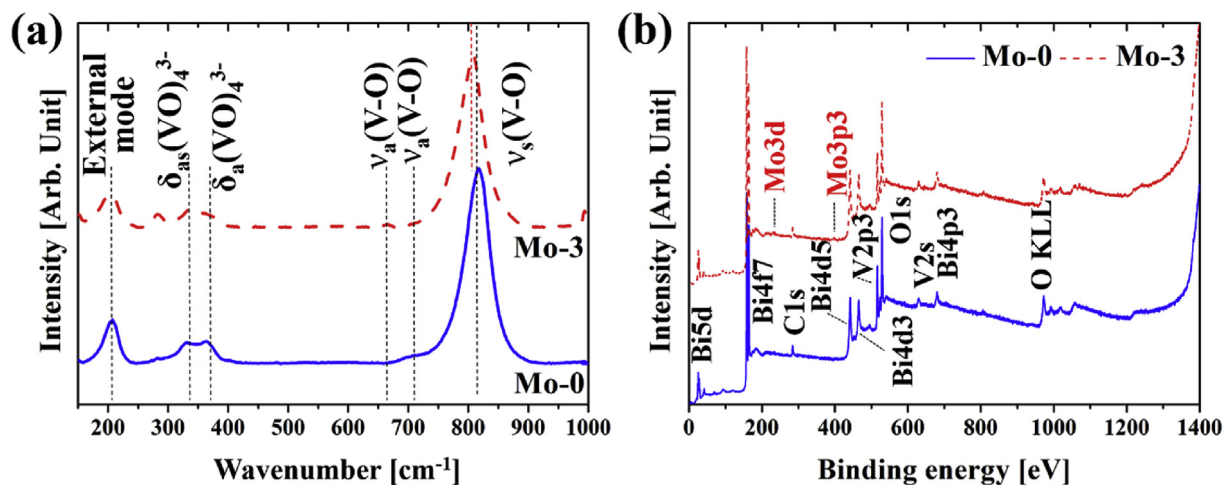


Fig. 4. (a) Raman and (b) XPS survey spectra of Mo-0 and Mo-3.

wavenumber (808 cm^{-1}) for the Mo-3 film compared to its position in the Mo-0 film. This shift is due to Mo^{6+} that substitutes V^{5+} in the BiVO_4 lattice. The diatomic approximation is used for bond length calculations assume a that vibrations of metal–oxygen bonds are independent of one another in the crystal lattice. The bond length of V–O can be calculated from the empirical equation given by Hardcastle et al. [38] based on Raman stretching frequencies. Here, the calculated V–O bond length increased from 1.659 to 1.678 Å for Mo-0 to Mo-3 respectively [20,39].

The valence states of all the constituent elements were investigated by XPS. Fig. 4b shows XPS survey spectra of the Mo-0 and Mo-3 films. Both spectra contain peaks related to the binding energies of Bi4f, V2p, and O1s. In addition, Mo-related peaks can be seen clearly at approximately 231 and 234 eV in the spectrum of Mo-3.

Fig. 5 shows the high-resolution scans for the individual core elements of the Mo-0 and Mo-3 films. Both films exhibit similar high-intensity Bi4f, V2p, and O1s peaks. However, there is a slight shift in binding energy in the case of Mo-3 owing to Mo doping. Fig. 5a shows that the Bi4f core level could be split into two peaks, Bi4f $_{7/2}$ and Bi4f $_{5/2}$, with binding energies of 158.2, and 163.6 eV, respectively. The V2p core level peaks, for V2p $_{3/2}$ and V2p $_{1/2}$, have binding energies of 515.8 and 523.5 eV, respectively, as can be seen from Fig. 5b. The Bi4f and V2p XPS peaks were in keeping with monoclinic scheelite-like BiVO_4 [10,22]. The O1s XPS spectra in Fig. 5c contain a peak at 529 eV, confirming the presence of metal oxide bonds. The doping of Mo^{6+} in BiVO_4 resulted in the Bi4f, V2p, and O1s peaks shifting to higher binding energies compared to their positions in BiVO_4 . These shifts are indicative of stronger interactions between the hexavalent dopant and Bi, V, and O owing to the high electronegativity of Mo^{6+} . As expected, Mo was detected only in case of Mo-3; the representative spin-orbit splitting of the Mo3d spectrum are shown in Fig. 5d. The Mo3d $_{3/2}$ and Mo3d $_{5/2}$ peaks located at 234.7 and 231.7, respectively, confirmed the presence of hexavalent Mo (Mo^{6+}). No additional peaks attributable to metallic Mo or Mo oxide were observed near 288.0 and 229.5 eV, confirming the successful doping of Mo in BiVO_4 [10].

3.2. Optical and photoelectrochemical properties

The absorbance spectra of the Mo-0 and Mo-3 films were measured using a UV–visible spectrometer; the results are shown in Fig. 6a. The absorption edges of BiVO_4 (Mo-0) and Mo-doped BiVO_4 (Mo-3) lie at 450–560 nm. The intensity of the absorption

edge increased with Mo doping, and it was slightly red-shifted. The optical band gap energies as determined from the linear part of the $(\alpha h\nu)^2$ versus photon energy ($h\nu$) plots shown in Fig. 6b suggest a slight lowering of the band gap from 2.32 to 2.2 eV upon doping. Comparing the calculated band gaps with that reported for monoclinic scheelite-like BiVO_4 (2.3 eV), we conclude that Mo doping decreased the band gap. The reduced bandgap of the Mo-doped BiVO_4 samples could allow them to absorb more photons and generate a greater number of electron-hole pairs as compared to the pristine BiVO_4 sample [9,40].

The PEC performances of the Mo-0 and Mo-3 films were evaluated by measuring the PCD; the results are shown in Fig. 7. The PCD values of the undoped and doped BiVO_4 films indicate that they had *n*-type characteristics. During the measurements, we used a “back illumination” geometry in which, light passes through the ITO-coated glass substrate. Therefore, the higher-energy photons are absorbed nearer to the ITO layer, whereas the lower-energy ones are absorbed over a longer distance, that is, farther from the ITO layer. In a porous structure, such as these films, the transport distance for holes is always short because holes only have to reach the film/electrolyte interface, where they are used for oxygen evolution. The potentials shown are with reference to the reversible hydrogen electrode (RHE), and an Ag/AgCl electrode, which are related by $E_{\text{RHE}} = E_{\text{Ag/AgCl}} + 0.059\text{ pH} + 0.1976$, where E_{RHE} is the potential versus the RHE, $E_{\text{Ag/AgCl}}$ is the potential versus the Ag/AgCl electrode, and pH is the potential of hydrogen value for Na_2SO_4 electrolyte solution [23].

The pristine BiVO_4 film (Mo-0) exhibited a PCD value of $0.9\text{ mA}\cdot\text{cm}^{-2}$ and zero dark current. When the Mo concentration was increased from 0 to 0.20%, the resulting Mo- BiVO_4 film exhibited a markedly higher PCD than that of the pristine BiVO_4 film. The PCD value increased with increasing Mo concentration up to sample Mo-3, with the maximum PCD value reaching $1.78\text{ mA}\cdot\text{cm}^{-2}$ at 1.2 V (versus Ag/AgCl). Thus, the PCD value of the Mo-3 film was twice that of the Mo-0 film. However, when the Mo concentration was increased further to 0.20% (Mo-4), the PCD value decreased to $0.95\text{ mA}\cdot\text{cm}^{-2}$. The reduction in PCD is attributed to formation of defects at higher Mo-doping, which acted as traps for electrons and holes and thus functioned as recombination centers [41]. The PCD values of the Mo- BiVO_4 films produced by ESD in this study are compared with those of previously reported films in Table 1. This comparison reveals that the films synthesized in this study exhibited significantly better PEC performance.

The transient photovoltage measured in open circuit (i.e. no

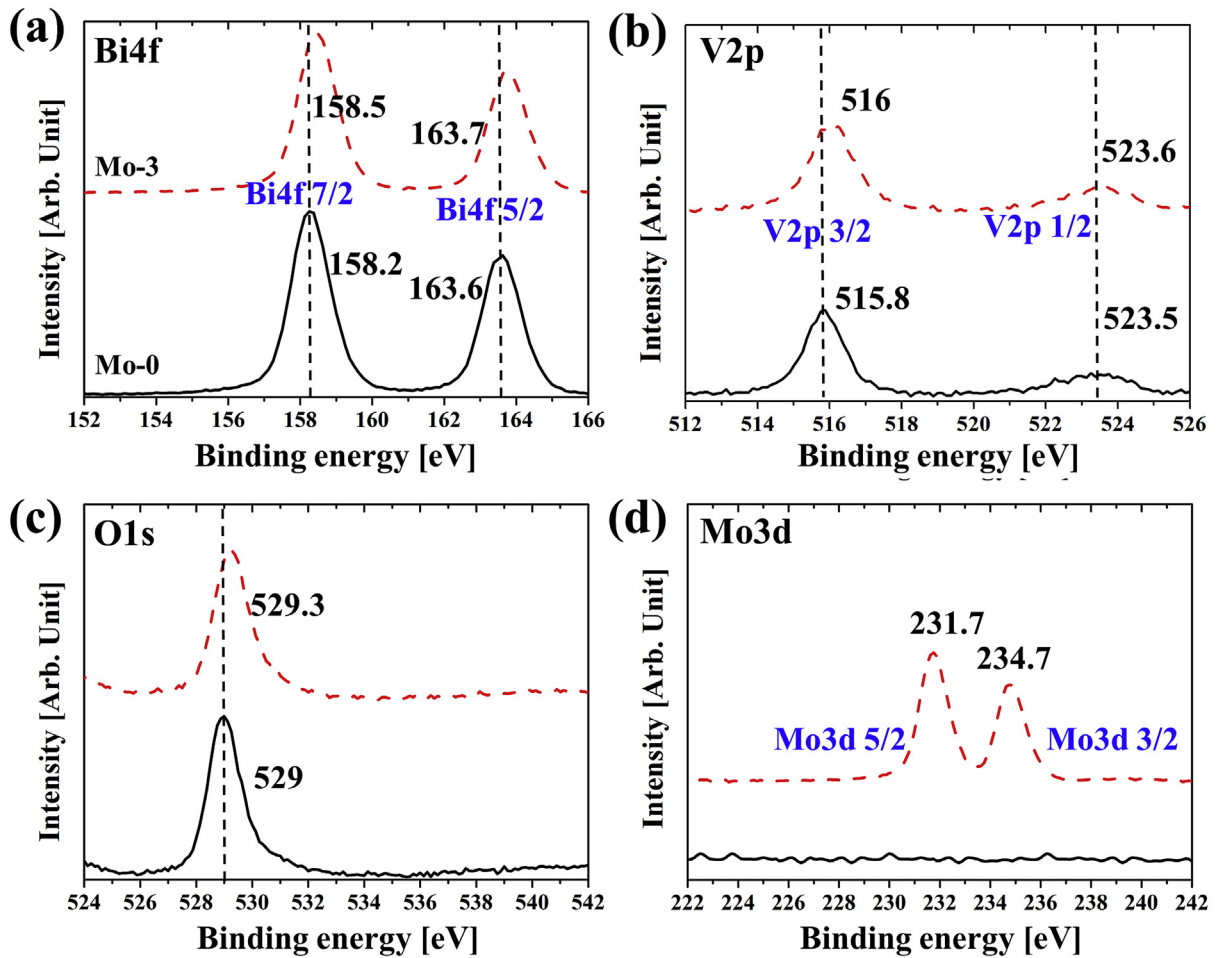


Fig. 5. High-resolution XPS spectra for (a) Bi4f (b) V2p (c) O1s, and (d) Mo3d energy ranges of Mo-0 (black line) and Mo-3 (red dotted line). (For interpretation of the references to colour in this figure legend, the reader is referred to the web version of this article.)

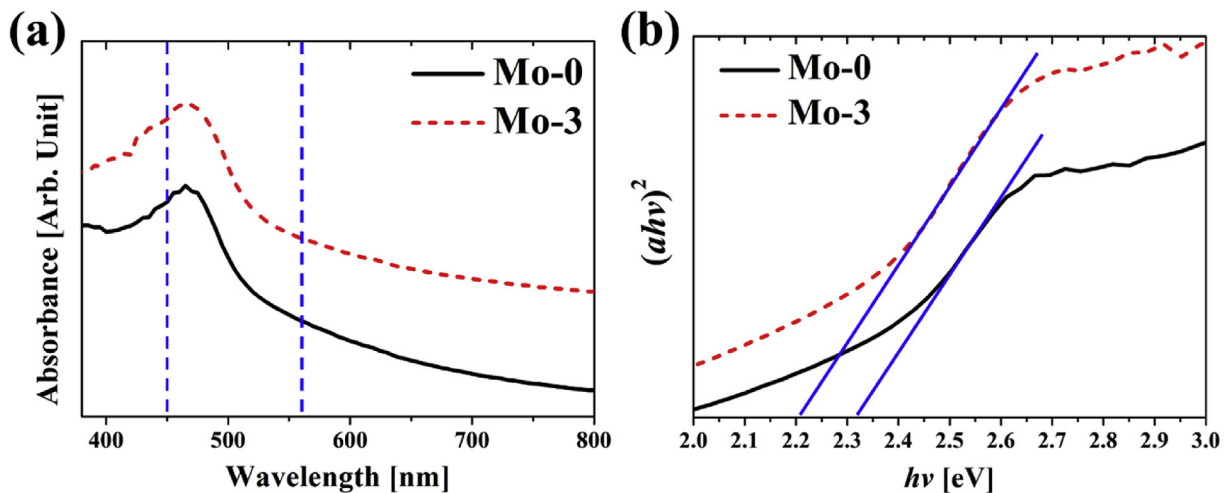


Fig. 6. (a) Absorption spectra and (b) band gap energies of Mo-0 and Mo-3.

applied bias) is shown in Fig. 8a. Under dark conditions, the electrode potential is determined by redox equilibrium. When the electrode is illuminated, photoexcited electrons accumulate at the electrode. The Fermi level is shifted toward lower voltage due to

this electron accumulation. Thus, a steady-state photovoltage is generated under illumination. Upon switching from the dark to illuminated state, or vice-versa, a transient in the photovoltage is observed, reflecting the time required for electron accumulation,

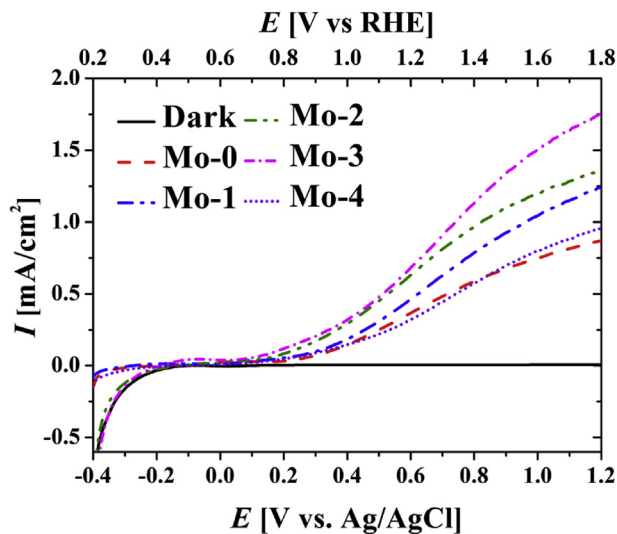


Fig. 7. Photocurrent density of different Mo-doped films in 1 M Na₂SO₄ as the electrolyte.

upon illumination, or electron relaxation back to the dark condition when illumination is stopped.

The photo-stability of the Mo-3 sample was tested by chronoamperometry. The photocurrent (0.32 mA cm⁻²) was measured at a potential of 0.5 V (vs. Ag/AgCl) and the results demonstrate high photostability even after 166 min under one-sun illumination (100 mW·cm⁻²) as shown in Fig. 8b. Thus stable photocurrent

confirms that Mo-BiVO₄ nanopillars remain intact under light illumination over a period of hours, and thus none of the photocurrent should be attributed to photocorrosion or other transient processes.

Fig. 9a shows the Bode phase plots as determined from the EIS measurements performed under back illumination. The frequency range for the analysis was 100 kHz to 100 mHz for all the samples. The charge transport time factor (τ_n) for electron recombination was determined from the characteristic frequency (f_m), which corresponded to the peak phase angle in the Bode phase plot. The charge transport time factor was calculated using the following equation:

$$\tau_n = \frac{1}{2\pi f_m} \quad (1)$$

With increasing Mo doping in BiVO₄, the characteristic frequency or the frequency corresponding to the peak phase angle in the Bode phase plot decreased, as shown in Fig. 9a. This shift was attributable to the fact that doping with Mo increased the donor concentration. However, in sample Mo-4, the characteristic frequency was higher; this may be due to the higher recombination rate associated with defects in this case. The charge transport time factor τ_n (ms) values shown in Fig. 9b confirm that the doping of Mo had a significant effect on the properties of BiVO₄. The charge transport time factor for electron recombination increased with an increase of Mo-doping from 0% to 0.15%, changing from 2 to 63 ms, as shown in Fig. 9b. However, for Mo-4, the charge transport time factor decreased to 40 ms; this can be ascribed to the formation of a greater number of defects in the BiVO₄ crystals, which promotes recombination. Further, that the charge transport time factor of

Table 1
Comparison of PEC performances of Mo-BiVO₄ films synthesized in present study with those reported in literature.

Method	Scan rate [mV/s]	Electrolyte	PCD [mA cm ⁻²]	Reference
Drop coating	25	0.1 M Na ₂ SO ₄	3.2 ^a	[19]
Spin coating	30	0.5 M Na ₂ SO ₄	0.35 ^b	[43]
Spin coating	10	0.1 M phosphate	1.2 ^b	[27]
Spin coating	25	0.5 M Na ₂ SO ₄	0.52 ^a	[44]
Spray coating	15	0.1 M Phosphate	1.2 ^a	[45]
Electrospinning	—	0.1M K-Pi	0.32 ^b	[24]
Electrostatic spray	10	0.5 M Na ₂ SO ₄	1.78 ^a	Present

^a PCD measured vs. Ag/AgCl.

^b PCD measured vs. RHE.

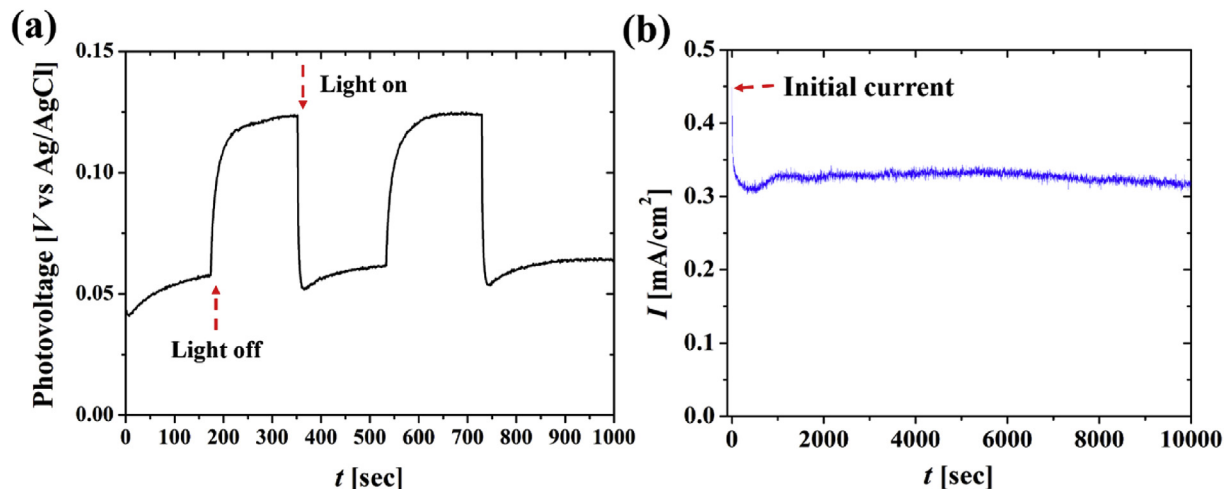


Fig. 8. (a) Photovoltage plot under dark and illuminated conditions, as indicated, (b) Photocurrent stability of Mo-3 film at a potential of 0.5 V (vs. Ag/AgCl).

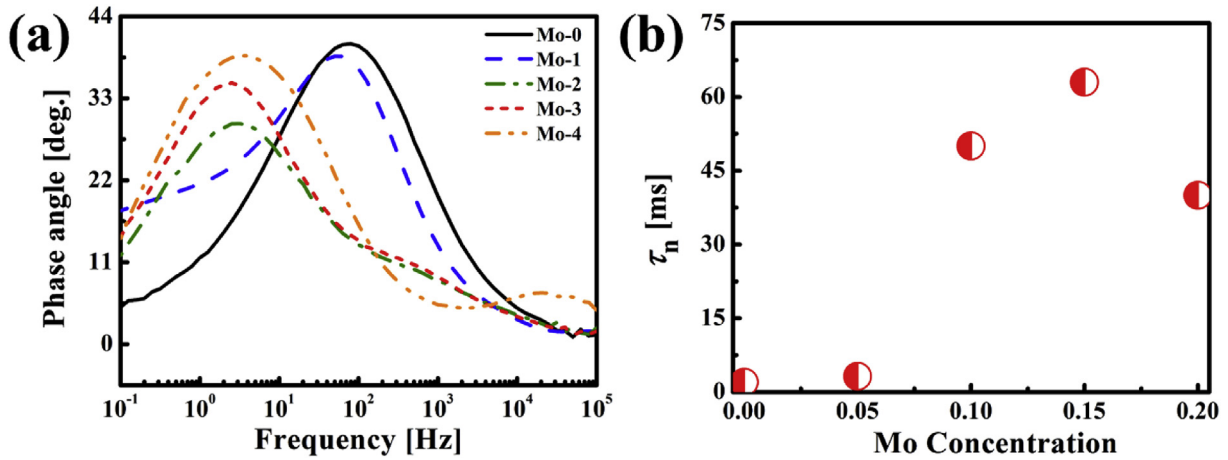


Fig. 9. (a) Bode phase plots of different Mo-doped BiVO₄ films and (b) Charge transport time factor values as determined from Bode phase plots for various Mo concentrations.

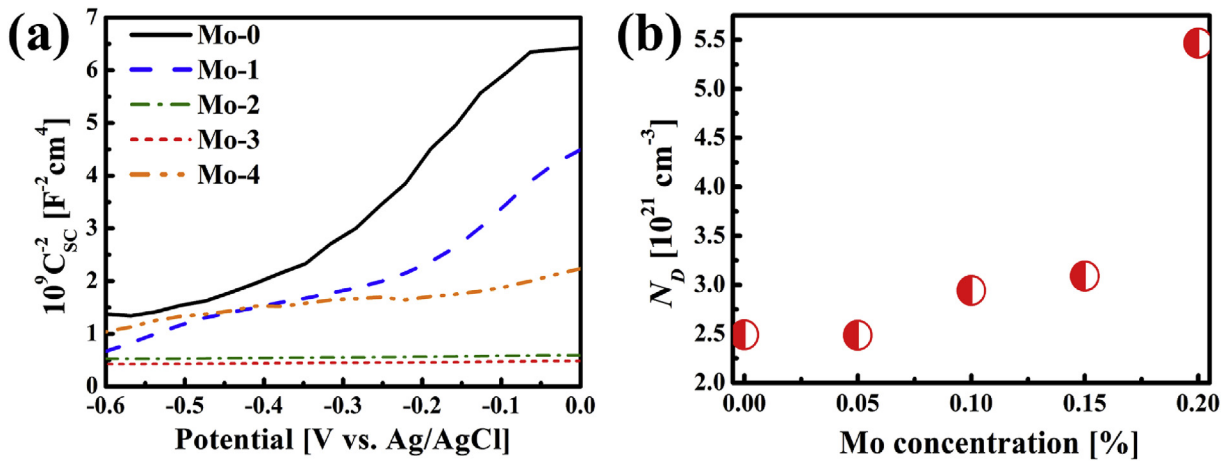


Fig. 10. (a) Mott-Schottky plots of different Mo-doped BiVO₄ films measured in 0.1 M Na₂SO₄ and (b) donor concentrations as determined from Mott-Schottky plots.

BiVO₄ was small can be attributed to the electron mobility in the conduction band being low. This poor charge transport is associated with the high activation energy required for the electrons to hop between the VO₄ tetrahedra. The doping of Mo results in crystal deformation, that is, changes in the crystal structure that can lower this activation energy. That leads to an increase in the electron

mobility and a decrease in the recombination rate [19]. Therefore, with the doping of a greater amount of Mo, the charge transport time factor increases. That explains the higher PCD values of the Mo-BiVO₄ films (see Fig. 7).

The electron mobility and charge transport time factor corresponding to electron recombination are both significantly affected

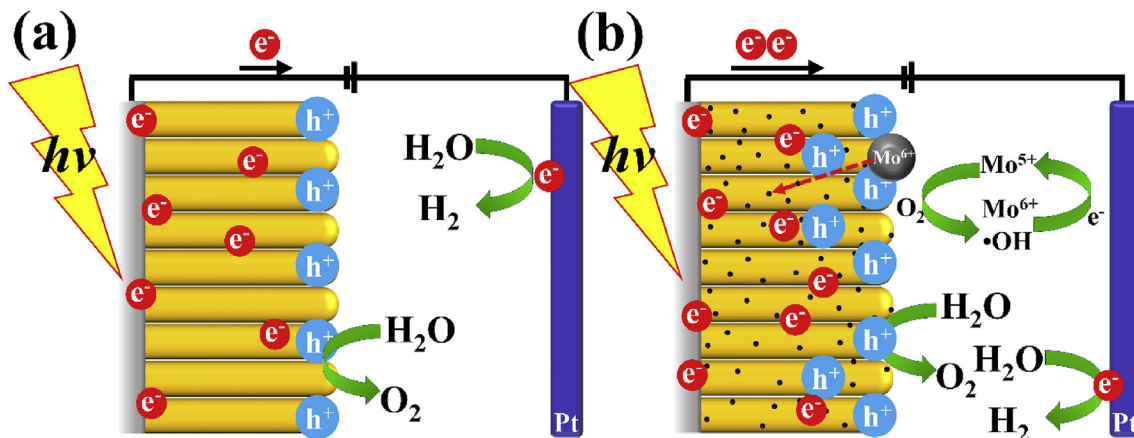


Fig. 11. Mechanism of charge separation in (a) BiVO₄ and (b) Mo-BiVO₄ photoanodes.

by the donor (electron) concentration. Hence, it was essential to study the changes in the donor concentration due to Mo doping in BiVO₄. To estimate the donor concentrations in the pristine and Mo-doped BiVO₄ films, Mott-Schottky characterizations were performed on samples Mo-0 to Mo-4 using 0.5 M Na₂SO₄ as the electrolyte and an Ag/AgCl electrode as the reference electrode. The Mott-Schottky measurements were conducted using an amplitude modulation of 10 mV under dark conditions; the applied potential range was 0 to –0.6 V, and the frequency was kept constant at 1000 Hz. The Mott-Schottky plots were obtained by assuming ideal semiconductor characteristics:

$$\frac{1}{C_{sc}^2} = \left(\frac{2}{e\epsilon\epsilon_0 N_D} \right) \left(\frac{E - E_{fb} - kT}{e} \right), \quad (2)$$

where E is the conduction band potential (V), E_{fb} is the flat band potential (V), k is the Boltzmann constant, T is the temperature (K), e is a charge of an electron (C), ϵ is the relative permittivity, ϵ_0 is the dielectric constant, N_D is the donor concentration per unit volume (cm⁻³), and C_{sc} is the surface charge capacitance (F cm⁻²).

The obtained Mott-Schottky plots are shown in Fig. 10a. These show that with increasing Mo-doping, the voltage-surface charge capacitance curve becomes more linear, indicating an increase in the donor concentration. The slope of the Mott-Schottky curve was used to determine the flat band potential (E_{fb}) of the corresponding sample based on the intercept of the tangent at the x -axis [42]. The flat band potential varied from 0.41 to 0.49 V. Further, these values of E_{fb} were used in the above equation to calculate the donor concentrations, as shown in Fig. 10b. We observed that the pristine BiVO₄ (Mo-0) film demonstrated a lower donor concentration as compared to the Mo-doped BiVO₄ samples. Thus, all the samples (Mo-0 to Mo-4) exhibited high donor concentrations, which ranged from 2.5×10^{21} cm⁻³ to 5.5×10^{21} cm⁻³. This further explains how Mo doping results in an increase in the PCD.

The mechanism responsible for the enhanced PCD of the Mo-BiVO₄ samples is described in Fig. 11. In the case of BiVO₄, when the light is irradiated from the back side, the electron-hole pairs separate, resulting in the oxidation of water, which is represented by the reaction. On the other hand, in the Mo-BiVO₄ samples, the electron concentration is higher, owing to the doping of hexavalent Mo. At the same time, the slightly distorted VO₄ tetrahedra allow for fast electron hopping. Further, the Mo⁶⁺-doped BiVO₄ traps a greater number of electrons and suppresses electron-hole recombination; this is owing to the dipole moment of the distorted tetrahedra and the Schottky barrier formed between ITO and Mo doped BiVO₄. Thus, a greater number of electrons are available for excitation under the visible light.

The mechanism presented in Fig. 11 shows that BiVO₄ can generate electron-hole pairs under illumination. However, doping with Mo has two synergistic effects; it provides additional free electrons and suppresses electron-hole pair recombination, thus ensuring a high PCD.

4. Conclusions

We fabricated Mo-BiVO₄ films with a structure consisting of three-dimensional porous nanopillars using the ESD method. The successful doping of Mo in BiVO₄ was confirmed by XPS analysis. Further, XRD analysis confirmed that the doped Mo dissolved in BiVO₄ without the formation of any secondary phases. The optical absorbance measurements showed that there was a slight shift in the absorption edge after doping with Mo; however, the total absorbance was enhanced by Mo doping. The doping of Mo in concentrations of up to 0.15% (Mo-3) increased the hole diffusion length, leading to a two-fold enhancement in the PCD under

simulated AM 1.5 sunlight as compared to that for pristine BiVO₄. This increase in the PCD is attributable to improved charge separation because of the doping of Mo in the optimized concentration. Finally, Mott-Schottky measurements revealed a shift in the position of the flat band in the case of the Mo-doped BiVO₄ samples.

Acknowledgement

This research was supported by the Technology Development Program to Solve Climate Changes of the National Research Foundation (NRF) funded by the Ministry of Science, ICT and Future Planning (2016M1A2A2936760), NRF-2013M3A6B1078879, and NRF-2017R1A2B4005639.

References

- [1] R. Marschall, Semiconductor composites: strategies for enhancing charge carrier separation to improve photocatalytic activity, *Adv. Funct. Mater.* 24 (2014) 2421–2440.
- [2] K. Kasinathan, J. Kennedy, M. Elayaperumal, M. Henini, M. Malik, Photodegradation of organic pollutants RhB dye using UV simulated sunlight on ceria based TiO₂ nanomaterials for antibacterial applications, *Sci. Rep.* 6 (2016).
- [3] J. Liqiang, Q. Yichun, W. Baiqi, L. Shudan, J. Baojiang, Y. Libin, F. Wei, F. Honggang, S. Jiazhong, Review of photoluminescence performance of nano-sized semiconductor materials and its relationships with photocatalytic activity, *Sol. Energy Mater. Sol. Cells* 90 (2006) 1773–1787.
- [4] Z. Zou, J. Ye, K. Sayama, H. Arakawa, Direct splitting of water under visible light irradiation with an oxide semiconductor photocatalyst, *Nature* 414 (2001) 625–627.
- [5] G. Longo, F. Fresno, S. Gross, U.L. Stangar, Synthesis of BiVO₄/TiO₂ composites and evaluation of their photocatalytic activity under indoor illumination, *Environ. Sci. Pollut. R.* 21 (2014) 11189–11197.
- [6] B. Sathyaseelan, E. Manikandan, V. Lakshmanan, I. Baskaran, K. Sivakumar, R. Lachumananandasivam, J. Kennedy, M. Maaza, Structural, optical and morphological properties of post-growth calcined TiO₂ nanopowder for optoelectronic device application: ex-situ studies, *J. Alloys Compd.* 671 (2016) 486–492.
- [7] R. Taziwa, E. Meyer, E. Sideras-Haddad, R. Erasmus, E. Manikandan, B. Mwakikunga, Effect of carbon modification on the electrical, structural, and optical properties of TiO₂ electrodes and their performance in lab-scale dye-sensitized solar cells, *Int. J. Photoenergy* 2012 (2012).
- [8] Y. Park, K.J. McDonald, K.-S. Choi, Progress in bismuth vanadate photoanodes for use in solar water oxidation, *Chem. Soc. Rev.* 42 (2013) 2321–2337.
- [9] S. Tokunaga, H. Kato, A. Kudo, Selective preparation of monoclinic and tetragonal BiVO₄ with scheelite structure and their photocatalytic properties, *Chem. Mater.* 13 (2001) 4624–4628.
- [10] C.M. Ghimbeu, E. Raymundo-Piñero, P. Fioux, F. Béguin, C. Vix-Guterl, Vanadium nitride/carbon nanotube nanocomposites as electrodes for supercapacitors, *J. Mater. Chem.* 21 (2011) 13268–13275.
- [11] D.K. Zhong, S. Choi, D.R. Gamelin, Near-complete suppression of surface recombination in solar photoelectrolysis by “Co-Pi” catalyst-modified W: BiVO₄, *J. Am. Chem. Soc.* 133 (2011) 18370–18377.
- [12] K.R. Tolod, S. Hernández, N. Russo, Recent advances in the BiVO₄ photocatalyst for sun-driven water oxidation: top-performing photoanodes and scale-up challenges, *Catalysts* 7 (2017) 13.
- [13] S. Balachandran, N. Prakash, K. Thirumalai, M. Muruganandham, M. Sillanpää, M. Swaminathan, Facile construction of heterostructured BiVO₄-ZnO and its dual application of greater solar photocatalytic activity and self-cleaning property, *Ind. Eng. Chem. Res.* 53 (2014) 8346–8356.
- [14] X. Zhang, B. Zhang, K. Cao, J. Brillet, J. Chen, M. Wang, Y. Shen, A perovskite solar cell-TiO₂/BiVO₄ photoelectrochemical system for direct solar water splitting, *J. Mater. Chem. A* 3 (2015) 21630–21636.
- [15] M.G. Mali, H. Yoon, M.-w. Kim, M.T. Swihart, S.S. Al-Deyab, S.S. Yoon, Electrospun heterojunction WO₃/BiVO₄ films with nanotextured pillar structure for enhanced photoelectrochemical water splitting, *Appl. Phys. Lett.* 106 (2015) 151603.
- [16] N. Micali, F. Neri, P.M. Ossi, S. Trusso, Light scattering enhancement in nanostructured silver film composites, *J. Phys. Chem. C* 117 (2013) 3497–3502.
- [17] H. Jung, S.Y. Chae, C. Shin, B.K. Min, O.-S. Joo, Y.J. Hwang, Effect of the Si/TiO₂/BiVO₄ heterojunction on the onset potential of photocurrents for solar water oxidation, *ACS Appl. Mater. Interfaces* 7 (2015) 5788–5796.
- [18] Q. Wang, T. Hisatomi, Q. Jia, H. Tokudome, M. Zhong, C. Wang, Z. Pan, T. Takata, M. Nakabayashi, N. Shibata, Scalable water splitting on particulate photocatalyst sheets with a solar-to-hydrogen energy conversion efficiency exceeding 1%, *Nat. Mater.* 15 (2016) 611–615.
- [19] B. Pattengale, J. Huang, The effect of Mo doping on the charge separation dynamics and photocurrent performance of BiVO₄ photoanodes, *Phys. Chem. Chem. Phys.* 18 (2016) 32820–32825.

- [20] V. Merupo, S. Velumani, G. Oza, M. Makowska-Janusik, A. Kassiba, Structural, electronic and optical features of molybdenum-doped bismuth vanadium oxide, *Mater. Sci. Semicond. process.* 31 (2015) 618–623.
- [21] E. Manikandan, V. Murugan, G. Kavitha, P. Babu, M. Maaza, Nanoflower rod wire-like structures of dual metal (Al and Cr) doped ZnO thin films: structural, optical and electronic properties, *Mater. Lett.* 131 (2014) 225–228.
- [22] K.P.S. Parmar, H.J. Kang, A. Bist, P. Dua, J.S. Jang, J.S. Lee, Photocatalytic and photoelectrochemical water oxidation over metal-doped monoclinic BiVO₄ photoanodes, *ChemSusChem* 5 (2012) 1926–1934.
- [23] H. Yoon, M.G. Mali, J.Y. Choi, M.-w. Kim, S.K. Choi, H. Park, S.S. Al-Deyab, M.T. Swihart, A.L. Yarin, S.S. Yoon, Nanotextured pillars of electrosprayed bismuth vanadate for efficient photoelectrochemical water splitting, *Langmuir* 31 (2015) 3727–3737.
- [24] H. Jung, S.Y. Chae, H. Kim, B.K. Min, Y.J. Hwang, Electrospun Mo-doped BiVO₄ photoanode on a transparent conductive substrate for solar water oxidation, *Catal. Commun.* 75 (2016) 18–22.
- [25] W.-J. Yin, S.-H. Wei, M.M. Al-Jassim, J. Turner, Y. Yan, Doping properties of monoclinic BiVO₄ studied by first-principles density-functional theory, *Phys. Rev. B* 83 (2011) 155102.
- [26] K. Ding, B. Chen, Z. Fang, Y. Zhang, Z. Chen, Why the photocatalytic activity of Mo-doped BiVO₄ is enhanced: a comprehensive density functional study, *Phys. Chem. Chem. Phys.* 16 (2014) 13465–13476.
- [27] H.W. Jeong, T.H. Jeon, J.S. Jang, W. Choi, H. Park, Strategic modification of BiVO₄ for improving photoelectrochemical water oxidation performance, *J. Phys. Chem. C* 117 (2013) 9104–9112.
- [28] L. Mingce, C. Weimin, Photoelectrochemical properties of BiVO₄ film electrode in alkaline solution, *Chin. J. Catal.* 29 (2008) 881–883.
- [29] L. Chen, E. Alarcón-Lladó, M. Hettick, I.D. Sharp, Y. Lin, A. Javey, J.W. Ager, Reactive sputtering of bismuth vanadate photoanodes for solar water splitting, *J. Phys. Chem. C* 117 (2013) 21635–21642.
- [30] M.-W. Kim, B. Joshi, H. Yoon, T.Y. Ohm, K. Kim, S.S. Al-Deyab, S.S. Yoon, Electrospun copper hexaoxidovanadate (CuV₂O₆) and pyrovanadate (Cu₂V₂O₇) photoanodes for efficient solar water splitting, *J. Alloys Compd.* 708 (2017) 444–450.
- [31] T. Lopes, L. Andrade, F. Le Formal, M. Gratzel, K. Sivula, A. Mendes, Hematite photoelectrodes for water splitting: evaluation of the role of film thickness by impedance spectroscopy, *Phys. Chem. Chem. Phys.* 16 (2014) 16515–16523.
- [32] T.W. Kim, K.-S. Choi, Nanoporous BiVO₄ photoanodes with dual-layer oxygen evolution catalysts for solar water splitting, *Science* 343 (2014) 990–994.
- [33] W. Yin, W. Wang, M. Shang, L. Zhou, S. Sun, L. Wang, BiVO₄ hollow nanospheres: anchoring synthesis, growth mechanism, and their application in photocatalysis, *Eur. J. Inorg. Chem.* 2009 (2009) 4379–4384.
- [34] L. Zhou, W. Wang, S. Liu, L. Zhang, H. Xu, W. Zhu, A sonochemical route to visible-light-driven high-activity BiVO₄ photocatalyst, *J. Mol. Catal. A Chem.* 252 (2006) 120–124.
- [35] H.S. Park, K.E. Kweon, H. Ye, E. Paek, G.S. Hwang, A.J. Bard, Factors in the metal doping of BiVO₄ for improved photoelectrocatalytic activity as studied by scanning electrochemical microscopy and first-principles density-functional calculation, *J. Phys. Chem. C* 115 (2011) 17870–17879.
- [36] S.M. Thalluri, R.M. Rojas, O.D. Rivera, S. Hernández, N. Russo, S.E. Rodil, Chemically induced porosity on BiVO₄ films produced by double magnetron sputtering to enhance the photo-electrochemical response, *Phys. Chem. Chem. Phys.* 17 (2015) 17821–17827.
- [37] S. Liu, K. Yin, W. Ren, B. Cheng, J. Yu, Tandem photocatalytic oxidation of Rhodamine B over surface fluorinated bismuth vanadate crystals, *J. Mater. Chem.* 22 (2012) 17759–17767.
- [38] F.D. Hardcastle, I.E. Wachs, Determination of vanadium-oxygen bond distances and bond orders by Raman spectroscopy, *J. Phys. Chem.* 95 (1991) 5031–5041.
- [39] S.M. Thalluri, C. Martinez Suarez, M. Hussain, S. Hernandez, A. Virga, G. Saracco, N. Russo, Evaluation of the parameters affecting the visible-light-induced photocatalytic activity of monoclinic BiVO₄ for water oxidation, *Ind. Eng. Chem. Res.* 52 (2013) 17414–17418.
- [40] R.P. Antony, P.S. Bassi, F.F. Abdi, S.Y. Chiam, Y. Ren, J. Barber, J.S.C. Loo, L.H. Wong, Electrospun Mo-BiVO₄ for efficient photoelectrochemical water oxidation: direct evidence of improved hole diffusion length and charge separation, *Electrochim. Acta* 211 (2016) 173–182.
- [41] J.A. Seabold, N.R. Neale, All first row transition metal oxide photoanode for water splitting based on Cu₃V₂O₈, *Chem. Mater.* 27 (2015) 1005–1013.
- [42] K. Gelderman, L. Lee, S. Donne, Flat-band potential of a semiconductor: using the Mott–Schottky equation, *J. Chem. Educ.* 84 (2007) 685.
- [43] X. Zhao, W. Luo, J. Feng, M. Li, Z. Li, T. Yu, Z. Zou, Quantitative analysis and visualized evidence for high charge separation efficiency in a solid-liquid bulk heterojunction, *Adv. Energy Mater.* 4 (2014) 1301785.
- [44] S.K. Pilli, T.E. Furtak, L.D. Brown, T.G. Deutsch, J.A. Turner, A.M. Herring, Cobalt-phosphate (Co-Pi) catalyst modified Mo-doped BiVO₄ photoelectrodes for solar water oxidation, *Energy Environ. Sci.* 4 (2011) 5028–5034.
- [45] S.K. Pilli, K. Summers, D. Chidambaram, Photoelectrochemical generation of hydrogen and electricity from hydrazine hydrate using BiVO₄ electrodes, *Phys. Chem. Chem. Phys.* 17 (2015) 13851–13859.